International Journal of Biological Macromolecules 309 (2025) 143118

Contents lists available at ScienceDirect

International Journal of Biological Macromolecules

journal homepage: www.elsevier.com/locate/ijbiomac

Structural and antigen-binding surface definition of an anti-CD93 monoclonal antibody for the treatment of degenerative vascular eye diseases

Luisa Raucci [a], Cosimo Damiano Perrone [a], Stefano Barbera [a,b], Laurens Julius de Boer [a,1], Gian Marco Tosi [c], Jlenia Brunetti [d], Luisa Bracci [d], Cecilia Pozzi [a,e,*], Federico Galvagni [a], Maurizio Orlandini [a,*,**]

[a] Department of Biotechnology, Chemistry and Pharmacy, University of Siena, Siena 53100, Italy
[b] Department of Immunology, Genetics and Pathology, Science for Life Laboratory, Uppsala University, Rudbeck Laboratory, Uppsala SE-75185, Sweden
[c] Department of Medicine, Surgery and Neuroscience, Ophthalmology Unit, University of Siena, Siena 53100, Italy
[d] Department of Medical Biotechnology, University of Siena, Siena 53100, Italy
[e] Consorzio Interuniversitario Risonanze Magnetiche di Metallo Proteine (CIRMMP), Sesto Fiorentino, FI 50019, Italy

ARTICLE INFO

Keywords:
Angiogenesis
Choroidal neovascularization
Multimerin-2
Crystallography
Molecular modeling

ABSTRACT

CD93 is a receptor predominantly expressed on the surface of endothelial cells, where it plays a pivotal role in angiogenesis through its interaction with the extracellular matrix. In our previous studies, we identified the monoclonal antibody 4E1 as a potent inhibitor of angiogenesis by targeting the CD93-Multimerin-2 axis. Here, we report the development of 4E1 as a recombinant whole immunoglobulin and a single-chain variable fragment, designated sc-4E. Both formats retained the binding properties of the parental monoclonal antibody and exhibited comparable inhibitory effects on endothelial cell migration and differentiation. To elucidate the molecular basis of the 4E1-CD93 interaction, we initially employed machine learning-based modeling and docking analyses of the variable heavy and light domains of 4E1. Subsequent crystallographic analysis of sc-4E provided high-resolution structural insights, confirming and validating the predicted model. Further docking experiments and molecular dynamics simulations using the crystallographic structures of CD93 and sc-4E revealed that the interaction is primarily mediated by the CDR-H3 and CDR-L2 loops. Notably, these regions engage with the sushi-like domain of CD93, which is critical for its interaction with Multimerin-2. This comprehensive structural and functional characterization of 4E1 and sc-4E underscores their potential as anti-angiogenic agents. By effectively inhibiting endothelial cell migration and differentiation, 4E1 derivatives represent promising therapeutic candidates for the treatment of ocular vascular diseases driven by pathological angiogenesis.

1. Introduction

Age-related macular degeneration (AMD) and diabetic retinopathy are two of the most common degenerative eye diseases characterized by excessive angiogenesis that cause severe vision loss in industrialized countries [1]. Although the current antiangiogenic therapy, based on intraocular injection of anti-VEGF drugs, provides significant visual benefits, it does not meet the needs of non-responders and/or patients undergoing frequent intravitreal injections to limit the recurrence of the disease [2]. Therefore, the discovery of new tools capable of blocking alternative proangiogenic pathways may assist in developing combination therapies to allow long-lasting clinical benefits by circumventing resistance mechanisms and avoiding the need for multiple treatments in patients [3].

Cluster of Differentiation 93 (CD93) is a single-pass transmembrane protein and a member of group 14 of the C-type lectin-like domain (CTLD) superfamily [4,5]. In recent years, CD93 has emerged as an ideal target for antiangiogenic therapy. Indeed, silencing experiments have

* Corresponding author at: Department of Biotechnology, Chemistry and Pharmacy, University of Siena, Siena 53100, Italy.
** Correspondence to: M. Orlandini, Department of Biotechnology, Chemistry and Pharmacy, University of Siena, Via A. Moro, 2, 53100 Siena, Italy.
E-mail addresses: cecilia.pozzi@unisi.it (C. Pozzi), maurizio.orlandini@unisi.it (M. Orlandini).
[1] Current address: COSYS/IMSE, Université Gustave Eiffel, 5 Boulevard Descartes Champs-sur-Marne, 77,454 Marne-la-Vallée, France.

https://doi.org/10.1016/j.ijbiomac.2025.143118
Received 24 January 2025; Received in revised form 9 April 2025; Accepted 10 April 2025
Available online 12 April 2025

highlighted the general involvement of CD93 in the regulation of endothelial cell (EC) function [6–8], CD93 has also been identified as one of the leading genes in tumor angiogenesis [9,10], and CD93 expression has been detected at high levels in hyperproliferative ECs, in contrast to the low expression in the healthy quiescent endothelium [11]. Importantly, the interaction between CD93 and the extracellular matrix pan-endothelial glycoprotein Multimerin-2 has been revealed to be crucial in the activation of CD93's proangiogenic signaling [12,13]. The binding of CD93 to Multimerin-2 promotes EC adhesion and tube formation and triggers the activation of β1 integrin during EC spreading and migration [14–16]. Intriguingly, CD93 and Multimerin-2 are both upregulated in the tumor vasculature during cancer progression and choroidal neovascularization [12,13,17,18], and their interaction, by stabilizing the cell surface expression of CD93, is involved in filopodia formation during tumor angiogenesis [16], suggesting that the CD93/Multimerin-2 interaction represents an ideal target to block pathological angiogenesis.

Previously, we generated a murine monoclonal antibody (clone 4E1, isotype IgG1k) against CD93, which proved effective in blocking angiogenesis without affecting the survival of quiescent ECs [6]. Moreover, in addition to demonstrating the key role played by CD93 in the formation of new blood vessels in the choroid, we showed that 4E1, by interfering with the binding of CD93 to Multimerin-2, exhibits anti-angiogenic activity in this tissue context [18]. Indeed, 4E1 recognizes a conformational epitope spanning the CTLD-sushi domains of CD93, the domains involved in the interaction with Multimerin-2 [12,19], reinforcing the hypothesis that hampering the CD93/Multimerin-2 interaction in the neovascularized choroid may offer potential benefits for the treatment of AMD patients.

In the present study we describe the development of 4E1 as a recombinant molecule and its inhibitory bioactivity on the migration and differentiation of primary ECs. Recognizing the importance of structural insights for antibody optimization, we employed machine learning-based structural modeling to predict and refine the 4E1-CD93 interaction. Advances in machine learning have significantly enhanced structural biology, enabling precise computational predictions of antigen-binding surfaces, guiding antibody engineering, and accelerating drug development [20,21]. Using bioinformatics-driven docking and molecular dynamics simulations, we characterized the molecular interactions between CD93 and engineered 4E1 derivatives. These computational approaches refined our antibody binding predictions, which were subsequently validated through X-ray crystallography. Starting from the amino acid sequence, we elucidated structural details of the 4E1 variable domains and investigate their interaction with CD93, ultimately leading to the development of a single-chain variable fragment (scFv), derived from 4E1 and termed sc-4E. scFvs represent a versatile and compact antibody format, retaining the antigen-binding capabilities of full-length antibodies while offering advantages such as ease of engineering and production [22]. The X-ray crystal structure characterization of sc-4E at 1.6 Å resolution enabled us to identify key amino acids contributing to the antibody-antigen interactions, providing crucial information for the future design of new tools to hamper the proangiogenic activity of CD93 in pathological contexts.

2. Materials and methods

2.1. DNA constructs

Total cellular RNA was extracted from hybridoma cells using the EuroGold Trifast Reagent (Euroclone, Pero, MI, Italy) following the manufacturer's instructions. Sequencing of the variable heavy (VH) and light (VL) chains of the mouse monoclonal antibody 4E1 was performed by Applied Biological Materials (abm, Richmond, Canada). The protein sequences of the VH and VL chains were determined, and the complementary-determining regions (CDRs) were identified using the *AbRSA* tool (http://cao.labshare.cn/AbRSA/index.html), according to the Chothia numbering scheme [23,24]. The VH-4e1 and VL-4e1 constructs, containing the respective VH and VL sequences of 4E1 optimized for expression in Chinese Hamster Ovary (CHO) cells and cloned into pBluescript vectors, were purchased from GenScript (Piscataway, NJ, USA). The plasmid for high yield production of rec4E1 in CHO cells was generated in two steps. First, the VH sequence from the VH-4e1 plasmid was subcloned into the *Age*I/*Afe*I sites of the pTRIOZ vector (InvivoGen, San Diego, CA, USA), generating the recombinant vector pT-VH4e1. Next, the VL sequence was PCR-amplified from the VL-4e1 plasmid and assembled into the *Pme*I/*Psh*AI sites of pT-VH4e1 using the NEBuilder HiFi DNA Assembly Cloning Kit (New England Biolabs, Ipswich, MA, USA), resulting in the expression vector pT-VHL4e1. All constructs were confirmed by DNA sequencing. The full-length human *CD93* cDNA (GenBank accession number NM_012072.4) cloned into pcDNA3 vector, the chimeric constructs expressing the Myc-tagged entire extracellular domain (pCS2-D1D3 vector) or the CTLD-sushi domains (pCS2-D1X vector) of CD93, and the D1X-pr construct for prokaryotic expression of the CTLD-sushi domains of CD93 (UniProKB, accession number Q9NPY3) were previously described [6,19]. The construct expressing the anti-CD93 scFv antibody (sc-4E) was purchased from GenScript. sc-4E was engineered in pET22b(+) vector by joining the VH and VL sequences from 4E1, optimized for expression in *E. coli* cells, using a $(Gly_4Ser)_3$ linker in the VH-linker-VL orientation. The construct includes a C-terminal 6×-His tag to facilitate purification and the pelB leader sequence to promote expression of the recombinant protein in the periplasmic space.

2.2. Cell culture and transfection

Hybridoma cells secreting the monoclonal antibody 4E1 were generated as previously described [6], and cultured in RPMI supplemented with 10 % fetal bovine serum (FBS) and 10 ng/mL human Interleukin-6 (OriGene Technologies, Rockville, MD, USA). CHO cells (ATCC, Manassas, VA, USA) were grown in DMEM supplemented with 10 % FBS, and transfectants were selected using complete medium containing 400 μg/mL Zeocin (InvivoGen). Human embryonic kidney (HEK) 293 cells (Thermo Fisher Scientific, Waltham, MA, USA) were cultured in DMEM with 10 % FBS and transfected in culture medium containing 2 % FBS and 1 mM sodium butyrate (Merck KGaA, Darmstadt, Germany). Primary human umbilical vein ECs (HUVECs) from pooled donors were purchased from Lonza (Walkersville, MD, USA) and grown on gelatin-coated plates in Endothelial Cell Basal Medium (EBM-2) with supplements, as previously described [25]. All cultures were confirmed to be mycoplasma-free by weekly testing. Transient transfection experiments were performed using the Transporter 5® Transfection Reagent (Polysciences, Warrington, PA, USA), following the manufacturer's instructions. To obtain soluble Myc-tagged CD93 proteins, HEK 293 cells were transiently transfected with either pCS2-D1D3 or pCS2-D1X plasmids. 24 h post-transfection, cells were rinsed with PBS and cultured in DMEM without supplements for 16 h. The supernatants were then clarified by centrifugation and used in Western blotting and solid-phase analyses.

2.3. Immunoblotting analysis

Western blotting was performed as previously described [26]. Under non-reducing conditions, protein samples were neither boiled nor treated with reducing agents prior to SDS-PAGE. The following antibodies were used for immunoblotting: mouse monoclonal 4E1, rec4E1, and sc-4E (600 ng/mL); mouse anti-Myc conjugated to horseradish peroxidase (HRP) (9E10, #sc-40, Santa Cruz Biotechnology, Dallas, TX, USA); mouse anti-His-HRP (#A7058) and mouse anti-β-actin (#MABT825, clone 4C2, Merck KGaA, Rahway, NJ, USA).

2.4. Protein expression and purification

To express the scFv antibody, *E. coli* BL21 (DE3) pLysS cells (Agilent, Santa Clara, CA, USA) were transformed with the plasmid encoding sc-4E. Bacterial cultures were grown in 1 L of ZYP-5052 auto-inducing medium at 20 °C with vigorous shaking for 48 h. Cells were harvested by centrifugation, resuspended in PBS supplemented with 250 mM NaCl, incubated with lysozyme (0.5 mg/mL) for 1.5 h on ice, and lysed by sonication. Following centrifugation at 11,000 x*g* for 1 h at 4 °C, samples from the total lysate, supernatant, and pellet were analyzed by SDS-PAGE and Coomassie staining to verify recombinant protein expression. Protein purification was performed using an AKTA Purifier fast protein liquid chromatography (FPLC) system equipped with a UV-900 detector and a Frac-900 fraction collector (Cytiva, Marlborough, MA, USA). sc-4E was purified by nickel-affinity chromatography using a HisTrap FF 5 mL column (Cytiva) and a step-gradient elution protocol with imidazole as the competitive eluting agent. The specific elution of sc-4E occurred at an imidazole concentration of approximately 250 mM. Fractions containing the target protein were identified by SDS-PAGE, pooled, and dialyzed against PBS. The final yield was approximately 15 mg of purified protein per liter of bacterial culture. For rec4E1 purification, protein A-affinity chromatography was performed using a HiTrap rProtein A FF 1 mL column (Cytiva). Antibody-containing supernatants from CHO cell cultures were centrifuged, filtered through a 0.45 μm filter, and diluted 1:1 with binding buffer (0.02 M sodium phosphate, 3 M NaCl, pH 7.0). Elution was carried out using 0.1 M sodium citrate (pH 3), and eluted fractions were immediately neutralized with 1 M Tris-HCl (pH 8.5), dialyzed against PBS, and concentrated using Centricon filters (Merck KGaA). Protein concentrations were determined using a NanoPhotometer N60 (Implen GmbH, Munchen, Germany). The D1X-pr mutant, containing the CTLD-sushi domains of human CD93, was expressed in *E. coli* and purified as previously described [19].

2.5. Binding kinetics by surface plasmon resonance

Binding analysis was performed using a BIAcore T200 (Cytiva). The 4E1, rec4E1, or sc-4E antibodies were immobilized *via* amine coupling onto a CM5 sensor chip following standard procedures. Briefly, antibodies, diluted in sodium acetate (pH 4.0) at a concentration of 10 μg/mL were injected over the activated dextran surface of the flow cells for 300 s. The surface was activated using a mixture of EDC-NHS for 300 s. After antibody injection, a pulse of Ethanolamine 1 M was used to neutralize activated groups. A reference flow cell (blank) was prepared in parallel using the same activation/deactivation steps but without antibody immobilization. Recombinant D1X-pr protein was diluted in HBS-EP+ buffer to different concentrations and injected over all flow cells at a flow rate of 60 μL/min for 180 s. Dissociation was monitored for 600 s, and the chip surface was regenerated with a short pulse of 10 mM glycine (pH 2.0). Kinetic parameters were calculated using a 1:1 L binding model with BiaT200 evaluation software 2.0.1.

2.6. Solid-phase binding assay

An ELISA-based solid-phase binding assay was performed as previously described, with minor modifications [12]. 96-well Maxisorp plates (Nalge Nunc International, Rochester, NJ, USA) were coated with 100 μL per well of culture supernatant containing the Myc-tagged extracellular domains of CD93. Plates were blocked with bovine serum albumin (BSA) before the addition of purified antibodies (30 ng per well). After washing with PBS containing 0.05 % Tween-20, either anti-His-HRP (Merck KGaA) or anti-mouse-HRP secondary antibodies were added. Following additional washing steps, *o*-phenylenediamine (Merck KGaA) substrate was added to detect color development. Optical density values were measured using an EnVision 2105 multimode plate reader (Perkin Elmer, Waltham, MA, USA).

2.7. Immunofluorescence

HUVECs or transfected HEK 293 cells were detached from culture plates by a non-enzymatic cell dissociation method [15], seeded onto gelatin-coated glass coverslips, fixed with 3 % paraformaldehyde, and processed as previously described [25]. sc-4E was detected using a rabbit monoclonal antibody anti-His-tag (#MA5–33032, Thermo Fisher Scientific), followed by incubation with Alexa Fluor 488-conjugated secondary antibodies (Thermo Fisher Scientific). Fluorescent images were captured using a Leica TCS SP2 AOBS confocal laser-scanning microscope. Differential interference contrast images were also collected.

2.8. Wound healing, tube formation, and choroid sprouting assays

The scratch test was performed as previously described with slight modifications [14]. Briefly, HUVECs were seeded in 24-well plates and cultured until reaching confluency. A straight scratch was created in the cell monolayer using a sterile pipette tip. The cultures were washed with PBS and grown in complete medium containing 500 nM rec4E1, sc-4E, or an unrelated control antibody (mouse IgG1 isotype control, #02–6100, Thermo Fisher Scientific). Formation of capillary-like tube structures on growth factor reduced Matrigel (BD Biosciences, Franklin Lakes, NJ, USA) was carried out as previously described [7]. Briefly, 100 μL of Matrigel mixed with 500 nM of each antibody were polymerized in 24-well plates. HUVECs, detached from culture plates using a non-enzymatic method, were seeded in complete growth medium containing 500 nM rec 4E1, sc-4E, or unrelated antibodies. Tube formation was monitored at different time points. Choroid sprouting assays (CSAs) were carried out as previously described [18]. Humanized CD93 mice (B-hCD93 mice), on a C57BL/6 background, were purchased from Biocytogen (Beijing, China). CSA experiments were approved by the Local Ethics Committee of the University of Siena and the Italian Ministry of Health (approval n. 820/2021-PR). Bright-field images of the scratch, tube formation, and CSA assays were acquired using the Celena® S Digital Imaging System (Logos Biosystems, Anyang, South Korea), and representative fields were selected for analysis. Wound closure/cell migration, tube length and branching, and CSA sprouting area were quantified using ImageJ software.

2.9. Modeling, docking, and molecular dynamics analyses

Three-dimensional models of the VH and VL domains of 4E1 were generated from its primary amino acid sequence using ABodybuilder2 and ABlooper bioinformatics tools [27,28]. ABodybuilder2 is a web-based tool that applies database search algorithms, whereas ABlooper is a Python-based command-line tool that uses an equivalent graph neural network to predict CDR loop structures (https://github.com/oxpig/ABlooper). Protein-protein structure prediction was performed using a two-step approach. First, the antibody model or crystal structure was assembled with the CTLD-sushi domain structure of CD93 (Protein Data Bank, PDB ID: 8A59) using the LightDock docking sofware [29]. Docking parameters are detailed in the Supplementary Materials. Before docking, heteroatoms that might interfere with calculations were removed from the PDB files using the pdb-tools suite (https://www.bonvinlab.org/pdb-tools/). Next, protein-protein interactions were analyzed using PDBsum [30], and binding validation was performed using the PRODIGY tool [31]. Structural comparison among models was carried out using the Root Mean Square Deviation (RMSD) metric calculated with Biopython (https://github.com/sarisabban/RMSD?search=1). Molecular dynamics simulations were carried out using GROMACS version 2024.3 with the CHARMM36 force field [32]. The Surfaces tool was used to analyze macromolecular interfaces [33]. All structural figures were generated using PyMOL (https://www.pymol.org/).

2.10. Crystallization

Monomeric and dimeric forms of sc-4E, separated by size-exclusion chromatography, were concentrated to 5.6 mg/mL and 9.6 mg/mL, respectively in 20 mM Tris-HCl (pH 7.2) and stored at 4 °C until use. Crystallization trials were carried out using the sitting-drop vapor diffusion technique [34]. >350 precipitant solutions from commercial crystallization screens (Hampton Research, Aliso Viejo, CA, USA; and Jena Bioscience, Jena, Germany) were tested. Drops consisting of equal volumes (1.5 μL each) of protein and precipitant solution were equilibrated against a 200 μL reservoir at room temperature. Crystal growth was observed with the Crystal Screen 2 solution 36 (4.3 M NaCl, 0.1 M HEPES, pH 7.5). Optimization was performed by varying the precipitant concentration (3.5–4.5 M NaCl) and the crystallization buffer (0.1 M Bis-Tris pH 5.5 and 6.0, 0.1 M ADA pH 6.5, 0.1 M HEPES pH 7.0 and 7.5, 0.1 M Tris-HCl pH 8.0 and 8.5, and 0.1 M BICINE pH 9.0). Protein crystals formed in conditions containing 3.9–4.5 M NaCl across a wide pH range, from acidic to basic. Hexagonal-shaped crystals were individually transferred to cryoprotectant solutions (precipitant supplemented with 20 % *v/v* ethylene glycol), then flash-frozen in liquid nitrogen.

2.11. Data collection, structure solution, and refinement

Single crystals of the monomeric and dimeric forms of sc-4E, grown at various pH values, were tested for X-ray diffraction using synchrotron radiation at the European Synchrotron Radiation Facility (ESRF, Grenoble, France; beamline ID30A-3), PETRA III (EMBL Hamburg, Germany; beamline P13), and Diamond Light Source (DLS, Didcot, UK; beamline I04). Full datasets were collected at 100 K using either an Eiger2 XE 16 M or Eiger1 X 4 M detector. X-ray diffraction data were integrated using XDS [35] and scaled with Aimless [36] from the CCP4 suite [37]. All crystals belonged to the trigonal space group $P3_221$, showing only minor variations in unit cell parameters, and the asymmetric unit contained a single protein chain. Data collection and processing statistics for representative crystals are reported in Table S1. The structure of sc-4E was solved by molecular replacement using MOLREP [38]. As a search model, the structure of a neutralizing scFv antibody targeting the SARS-CoV-2 RBD (PDB ID: 7DET), which shares 74 % sequence identity, was used after removing all non-conserved and non-protein atoms. All structures were refined using REFMAC5 [39] from the CCP4 suite. Automatic rebuilding of missing atoms and water placement were performed using the ARP/wARP suite [40]. Manual model building and refinement were conducted between cycles using the Coot molecular graphic software [41]. Upon completion of the structural models, Fourier difference maps revealed the presence of two sodium cations bound to the protein, along with two to six chloride anions, one imidazole, and two to three ethylene glycol molecules, likely originating from the purification, crystallization, and cryoprotection solutions. Final models were manually inspected and validated using Coot and PROCHECK [42]. Refinement statistics for the most representative structures are summarized in Table S2. Structural figures were generated using CCP4mg [43]. Final coordinates and structure factors were deposited in the PDB under the accession codes: 9HY2 (sc-4E crystallized at pH 7.5, monomeric state from gel filtration), 9HY1 (sc-4E crystallized at pH 7.5, dimeric state from gel filtration), 9HY3 (sc-4E crystallized at pH 5.5), and 9HY5 (sc-4E crystallized at pH 9) (Tables S1 and S2).

2.12. Statistical analysis

Statistical analyses were performed using Prism software (GraphPad, San Diego, CA, USA). Data are expressed as mean ± SD from at least three independent experiments. The Shapiro-Wilk test was used to assess the normality of data distribution. For comparison between two groups, statistical significance was determined using the Student *t*-test for normally distributed values, or the Mann-Whitney *U* test for non-normally distributed data. All *P* values were two-tailed, and a value of *P* less or equal to 0.05 was considered statistically significant.

3. Results

3.1. Engineering and binding activity of recombinant 4E1

Since the production of antibodies by hybridoma technology is expensive, time-consuming, and sometimes cultured hybridoma cells can be subjected to mutations or gene loss over time, therapeutic antibodies are usually expressed as recombinant proteins [44]. To explore this possibility for the antibody 4E1, the mRNAs extracted from hybridoma cells and coding for the VH and VL chains were sequenced, and the amino acid sequences deduced (Table 1). To express an accurate ratio of heavy and light chains necessary for successful secretion of a whole antibody, the VH and VL sequences of 4E1 were subcloned into a vector specifically designed for high-yield production of whole recombinant murine monoclonal antibodies. We therefore generated the pT-VHL4e1 plasmid able to express a recombinant IgG1k (namely rec4E1) containing the VH and VL chains of 4E1. Importantly, the constant region of the H chain from rec4E1 carries the T252M mutation, which increases antibody affinity for Protein A and facilitates further purification steps. Next, CHO cells were transfected with the pT-VHL4e1 plasmid and selected in a Zeocin-containing culture medium. Cell supernatant was collected and subjected to Protein A-affinity chromatography (Fig. S1A). Eluted fractions were pooled, dialyzed, concentrated, and analyzed by SDS-PAGE and Western blot analysis, which confirmed specific purification free of contaminants of rec4E1 (Fig. S1B and S1C). To investigate whether rec4E1 had retained the same ability as 4E1 to recognize human CD93, we first expressed the previously described soluble CD93 deletion mutants containing the 4E1-recognized epitope [6] in HEK 293 cells and performed immunoblotting analyses to compare the binding activity of both antibodies. Importantly, rec4E1 recognized the CD93 deletion mutants, but only under non-reducing conditions (Fig. 1A), suggesting that like 4E1, rec4E1 recognizes a conformational epitope. Next, HEK 293 cells, which do not express endogenous CD93 [6], were transfected with a construct expressing full-length human CD93. rec4E1 bound CD93 both in the cell lysates and on the surface of cultured cells (Fig. 1B and C). Notably, rec4E1 also recognized endogenous CD93 expressed on HUVECs. In immunofluorescence analyses, it stained large $CD93^{+ve}$ vesicles formed during CD93 endocytosis and recycling in late spreading ECs [14] (Fig. 1D). Taken together, these results suggest that rec4E1 exhibits the same binding properties as 4E1.

3.2. Engineering and binding activity of the rec4E1-based scFv

Since scFvs have been shown to be valid substitutes for full-length antibodies in therapeutical, diagnostic, and biotechnological applications [45], we wondered whether 4E1 could be developed as a scFv antibody. To explore this possibility, the DNA sequences of VH and VL chains from 4E1, deprived of the leader sequences, were joined together by a linker sequence and the resulting recombinant molecule (namely sc-4E), optimized for bacterial expression, was cloned into pET22b(+) vector (Fig. S2). Although exogenous protein expression was assayed varying different parameters, in every condition, the recombinant sc-4E was expressed both in the insoluble and soluble fractions (Fig. S3A). Since the recovery of proteins from inclusion bodies is challenging [46], sc-4E was successfully purified by nickel-affinity chromatography only from the soluble fraction (Fig. S3B and S3C). To assess whether sc-4E had retained the ability to bind human CD93, we first analyzed its reactivity against the CD93 soluble deletion mutants. Immunoblotting analyses showed that sc-4E recognized the CD93 conformational epitope by binding the deletion mutants only under non-reducing conditions (Fig. 2A), but with a slightly decreased binding strength in comparison to rec4E1, as highlighted by the binding analysis in solid phase assays (Fig. 2B). These differences in binding strength were confirmed by

Table 1
VH and VL protein sequences of the monoclonal antibody 4E1.

VH sequence	
MGWSCIILFLVATATGVHSQEQLQQPGTELVKPGASVRLSCKTSGYTFASYTLHWVKQTPGQGLDWIGAIYPGNGDTSYNQKFKDKATLTADKSSSTAYMQLSNLTSEDSAVYYCARLDWYFDLWGAGTTVTVSA	
VL sequence	
MEFHDPILLWVLLLWVPGSTGDIVLTQSPTSLAVSLGQRATISCKASQSVDYDGDSYMNWYQQKPGQPPRLLIYAASNLESGIPARFSGSGSGTDFTLNIHPVEEEDAATYYCQQNNEDPRTFGGGTKLEIK	
	VH
CDR-1	GYTFASY
CDR-2	YPGNGD
CDR-3	LDWYFDL
	VL
CDR-1	KASQSVDYDGDSYMN
CDR-2	AASNLES
CDR-3	QQNNEDPRT

The complementary determining regions (CDRs) were determined according to the Chothia numbering scheme. The bold characters indicate the leader sequences.

surface plasmon resonance analysis, which calculated an affinity constant of 4.50×10^{-10}, 5.09×10^{-12}, and 2.80×10^{-11} for 4E1, rec4E1, and sc-4E respectively (Table 2 and Fig. S4). However, immunofluorescence analysis of HEK 293 cells transfected with a construct expressing human full-length CD93 showed the binding of sc-4E only to the surface of CD93-expressing cells (Fig. 2C), and importantly, immunoblotting and immunofluorescence analyses showed that sc-4E detected endogenous CD93 expressed in HUVECs (Fig. 2D and E), confirming that sc-4E binds CD93 similarly to rec4E1 and 4E1.

3.3. Functional analysis of rec4E1 and sc-4E

Since, we previously demonstrated the ability of 4E1 to impair the pro-migratory activity exerted by CD93 in the activated endothelium, we speculated that the rec4E1 and sc-4E antibodies were also able to inhibit EC migration. To address this question, we performed scratch assays, treating the cells with recombinant antibodies using the same concentration by which 4E1 inhibited EC proliferation and migration [6]. In contrast to the use of an unrelated antibody, rec4E1 and sc-4E impaired the ability of HUVECs to heal a wound (Fig. 3A and B). Further, while in the presence of unrelated antibodies, HUVECs formed a complete network of tubular-like structures, the treatment with rec4E1 or sc-4E abrogated the cells' capability to differentiate in tube-like structures on Matrigel (Fig. 3C and D). To determine whether rec4E1 and sc-4E, like 4E1, play an inhibitory role in choroidal vascularization, we utilized the *ex vivo* CSA, a well-established and reproducible model of choroidal angiogenesis [47]. Notably, experiments using choroidal tissue from CD93-humanized mice revealed that, unlike an unrelated antibody, 4E1 derivatives significantly inhibited the formation of endothelial sprouts (Fig. 3E and F). Taken together, these findings confirm that, like 4E1, both rec4E1 and sc-4E exhibit strong inhibitory activity against the proangiogenic function of CD93.

3.4. Modeling of the 4E1-CD93 interacting surfaces

To identify the amino acid residues critical for the 4E1-CD93 binding, we first modeled the structure of the VH and VL domains of 4E1 using bioinformatic tools based on machine learning techniques [27,28]. To this end, we obtained the 3D structure of 4E1 by matching previously resolved antibody structures deposited in the PDB, and we then accurately modeled the CDRs, generating the 4E1 model (4E1m) (Fig. 4A). To predict the structure of the 4E1-CD93 interacting surface, we docked the previously described crystal structure of CD93 [19] with 4E1m using LightDock and obtained a potential interacting complex (Fig. 4B). However, PDBsum analysis of the docked complex identified amino acid interactions primarily outside the CDRs, mainly localized in the VL chain of 4E1, as confirmed by molecular dynamics analyses (Fig. S5). Consequently, protein-protein interactions in the docked complex were analyzed using the PRODIGY tool, followed by molecular dynamics simulations to assess the stability of the identified interactions. The analyses of the interacting complex, characterized by high binding strength (ΔG, −11.6 kcal/mol), identified the CDRs primarily involved in the binding to CD93 (Fig. 4C and Table 3), with the significant observation that only three of the CDRs were directly engaged in the interaction. These results were further validated by analyzing the interacting interfaces of the 4E1m-CD93 complex by using the Surfaces tool (Fig. 4D) [33].

3.5. sc-4E crystal structure

To gain deeper insights into the interaction between the 4E1 CDRs and CD93, we utilized sc-4E for crystallographic analysis. Since we separated monomeric and dimeric states of sc-4E using size exclusion chromatography, each sample was crystallized individually. Despite a slight difference in concentration, they crystallized under the same conditions, forming hexagonal-shaped crystals that belonged to the

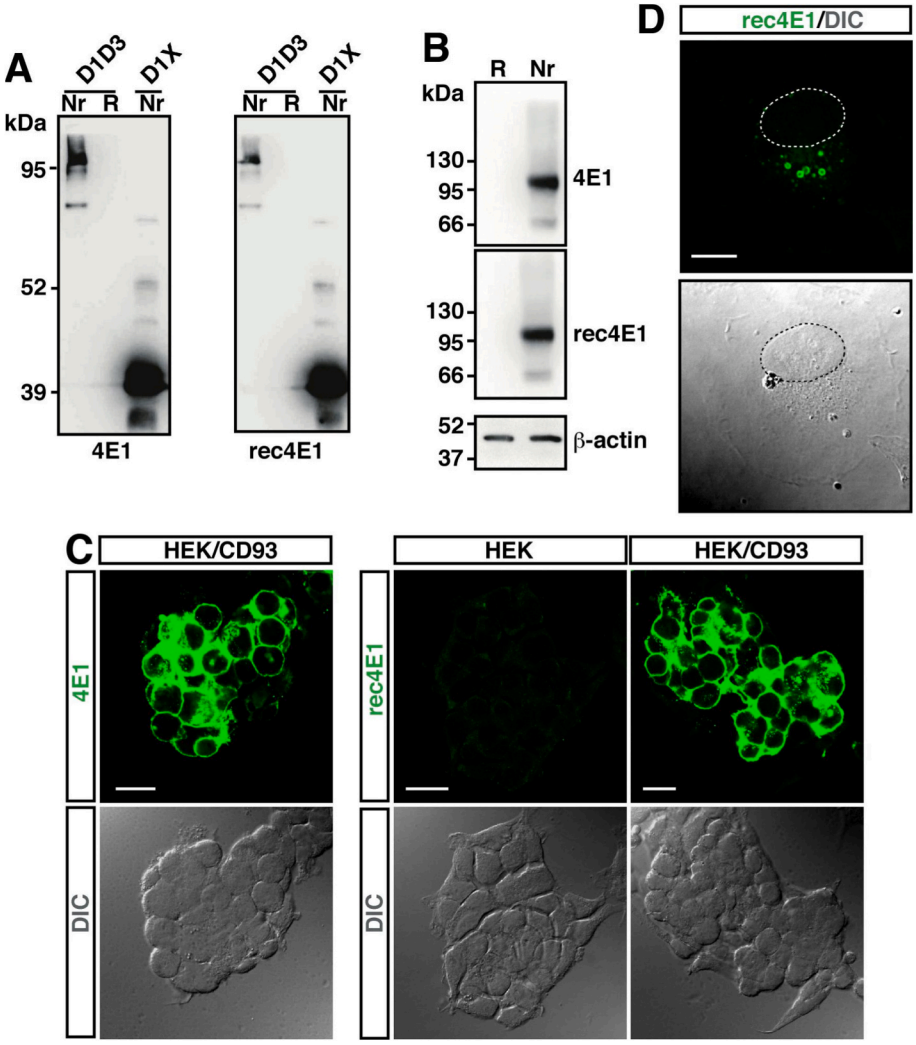

Fig. 1. rec4E1 binds to CD93. A: Immunoblot analysis of cell supernatants from HEK 293 cells transfected with vectors expressing the soluble deletion mutants of CD93 (D1X and D1D3), using 4E1 and rec4E1 antibodies. Cell supernatants were subjected to electrophoresis under reducing (R) or non-reducing (Nr) conditions. The D1X and D1D3 mutants correspond to amino acid residues 1–257 and 1–580, respectively of the human CD93 sequence. B: Cell extracts from HEK 293 cells transfected with a vector expressing full-length CD93 were separated by SDS-PAGE under non-reducing conditions and subjected to immunoblotting using 4E1 and rec4E1 antibodies. Anti-β-actin antibodies were used to confirm equal loading. C: Full-length CD93 was transiently transfected into HEK 293 cells (HEK/CD93). Fixed cells were analyzed by immunofluorescence using 4E1 and rec4E1 antibodies as indicated. Cells transfected with an empty vector (HEK) served as a control. Scale bars, 20 μm. D: Exponentially growing HUVECs were detached from the plate, resuspended in complete growth medium, plated on the substrate, and fixed at late stages of spreading. Cells were analyzed by immunofluorescence using the rec4E1 antibody. Dotted lines indicate nucleus boundaries. Scale bar, 12 μm. Differential interference contrast (DIC) images are shown.

trigonal space group $P3_221$, with only minor variations in unit cell parameters (Table S1). The structures were solved at resolutions of 1.70 Å (monomeric) and 1.81 Å (dimeric) and their comparison showed no meaningful changes in protein folding (RMSD upon Cα matching of 0.19 Å). Moreover, the analysis of the protein assembly with the PDBePISA tool [48] revealed the lack of specific interchain interactions that could lead to the formation of stable quaternary structures (Fig. S6A). In all crystals, the asymmetric unit (ASU) contained a single protein chain fully rebuilt, except for the starting two N-terminal residues, the segment 121–133, belonging to the flexible peptide linker, and the non-cleavable C-terminal His-tag. From the N- to C-terminus, the VH and VL regions are folded in nine strands (abcc'c"defg) forming two sheets in a sandwich-like structure (Fig. 5A). In both regions, a buried disulfide bridge (VH C24-C98 and VL C157-C226), spanning about 70 residues, connects strands b and f (Fig. 5A and B). These disulfide bridges are oriented roughly perpendicular to the individual sheets and significantly stabilize the folded domains. Two sodium cations, originating from the precipitant and cryoprotectant solutions, are bound to the crystal structure. The first sodium cation (Na1) is anchored to S79 in the VH, and its octahedral coordination sphere is completed by five water molecules (Fig. 5B). The second sodium cation (Na2) bridges the VL S141 and the VH Y104' of a symmetry related molecule, contributing to the stabilization of the crystal packing. Na2 is also octahedrally coordinated by four additional water molecules (Fig. 5B).

After identifying the first crystallization condition at pH 7.5, we screened different buffers, ranging from pH 5.5 to pH 9.0. Crystal formation was observed under all tested pH conditions. All single crystals displayed similar diffraction patterns with a maximum resolution ranging from 2.14 to 1.60 Å. The strongest diffractions were recorded from crystals grown at pH 5.5 and 9.0, allowing us to solve their structures at 1.62 Å and 1.60 Å resolution, respectively (Table S1 and S2). The comparison between the structures of sc-4E crystallized at pH 7.5 and those obtained from crystals grown at pH 5.5 and pH 9.0 shows no meaningful changes in protein folding (RMSD upon Cα matching of 0.18 Å and 0.19 Å, respectively) (Fig. S6B and S6C).

The sc-4E crystal structure highlights the putative interaction region

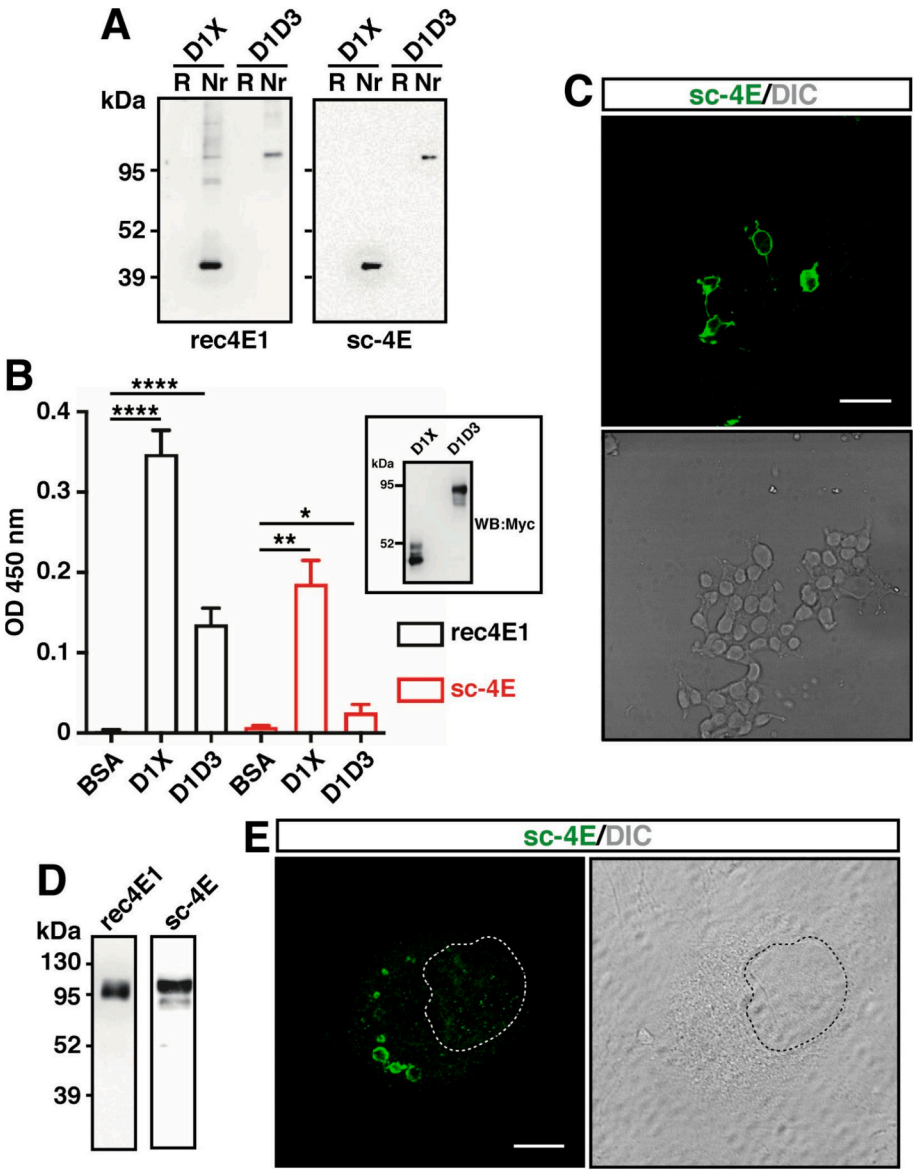

Fig. 2. sc-4E recognizes CD93. A: Immunoblot analysis of cell supernatants from HEK 293 cells transfected with vectors expressing the soluble Myc-tagged deletion mutants of CD93 (D1X and D1D3), using rec4E1 and sc-4E antibodies as indicated. Cell supernatants were subjected to electrophoresis under reducing (R) or non-reducing (Nr) conditions. B: Solid phase analysis of rec4E1 and sc-4E binding to soluble CD93 deletion mutants. Purified antibodies were applied to wells coated with CD93 deletion mutants (D1X and D1D3) or BSA, used as a control. Western blot analysis of the supernatants using an anti-Myc antibody is shown in the inset. SDS-PAGE was performed under reducing conditions. $^{****}P < 0.0001$ and $^{*}P < 0.05$; unpaired *t*-test. $^{**}P < 0.01$; Mann-Whitney test. C: CD93-transfected HEK 293 cells were analyzed by immunofluorescence using the sc-4E antibody. To visualize both transfected and non-transfected cells within the same microscope field, cells were transiently transfected with suboptimal concentration of the plasmid expressing full-length CD93. A differential interference contrast (DIC) image is shown. Scale bar, 40 μm. D: Western blot analysis of cell lysates from exponentially growing HUVECs, separated under non-reducing conditions, using rec4E1 and sc-4E antibodies. E: Immunofluorescence analysis of late spreading HUVECs using the sc-4E antibody. A DIC image is shown. Dotted lines indicate nucleus boundaries. Scale bar, 10 μm.

with CD93 (Fig. 6A). All CDRs are located on the same side, creating an extended surface optimized for recognizing the CD93 counterpart. The peculiar residue distribution in the CDRs generates a mostly hydrophobic interacting surface, with small negatively charged areas in the CDR—H2, CDR-L1, and CDR-L3 (Fig. 5B). The CDRs are folded as loops and analysis of the atomic B-factors in the structure reveals that they exhibit limited flexibility (Fig. 6C). Indeed, the atomic B-factors of the residues forming these regions are close to the average protein B-factor. The only exception is the central part of the CDR-L1, which shows a slightly increased flexibility.

Table 2
Kinetic association (ka) and dissociation (kd) and affinity constant (KD) of antibodies.

sample	ka	kd	KD
4E1	8.41×10^{4}	3.78×10^{-5}	4.50×10^{-10}
rec4E1	3.73×10^{6}	1.90×10^{-5}	5.09×10^{-12}
sc-4E	1.76×10^{6}	5.07×10^{-5}	2.80×10^{-11}

3.6. *sc-4E-CD93 interaction analysis*

The comparison between 4E1m and the crystal structure of sc-4E revealed an excellent structural matching. The CDRs exhibited a strong alignment with the crystal structure, indicating high confidence in the predictive accuracy of the model. Only the CDR-H3 loop emerged as the region with the most significant structural deviation (Fig. S7).

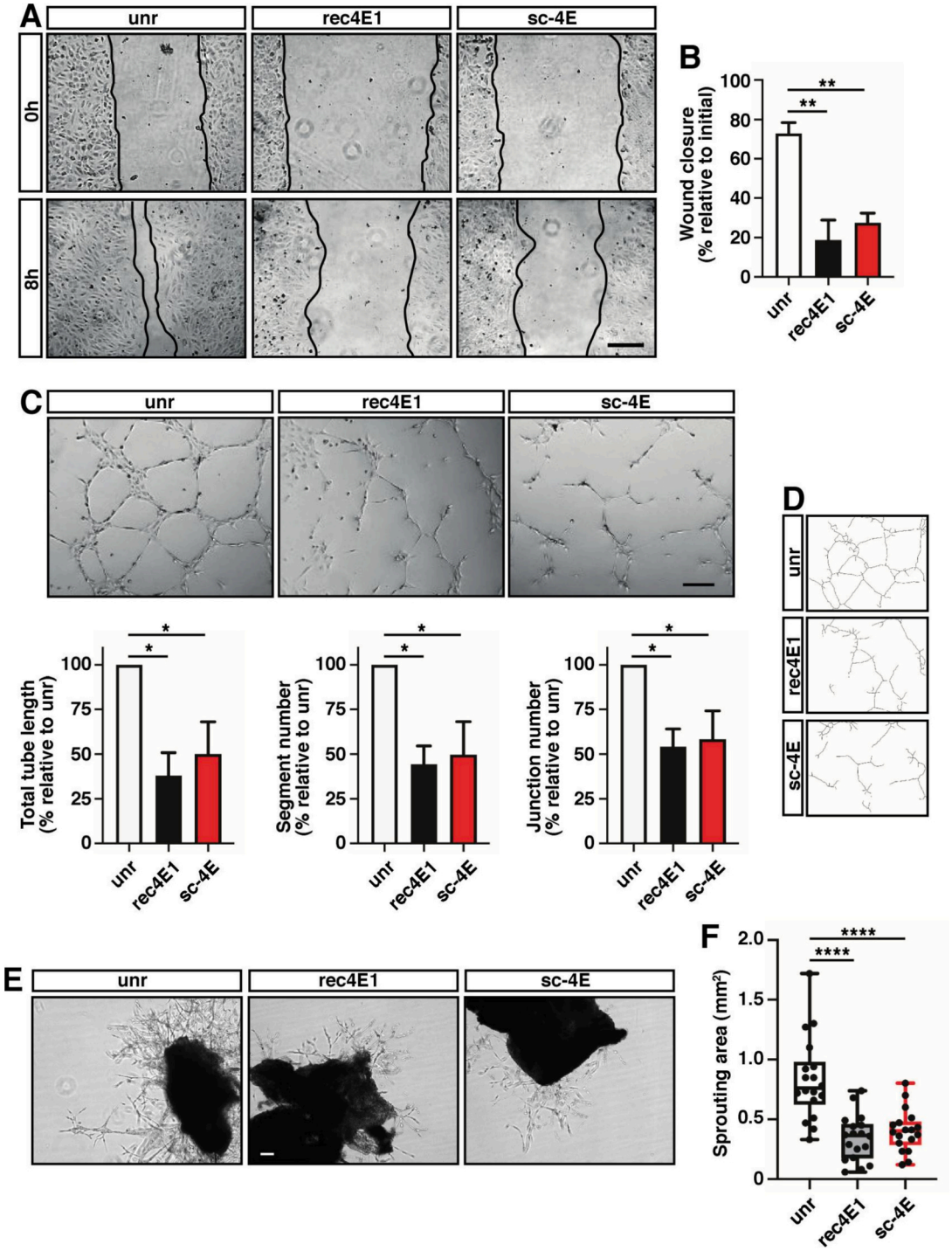

Fig. 3. rec4E1 and sc-4E affect migration and differentiation of human ECs. A: Representative images of wound closure in HUVECs treated with rec4E1, sc-4E, or unrelated (unr) antibodies. Cells were photographed at 0 and 8 h after the scratch. Scale bar, 100 μm. B: The percentage of wound closure was quantified using ImageJ and the Wound Healing Size Tool plug-in from images acquired at time 0 and 8 h in scratch experiments performed as in A ($n = 3$ images per conditions pooled from three independent experiments). $^{**}P < 0.01$; paired *t*-test. C: Representative images of a Matrigel tube formation assay. HUVECs were seeded on Matrigel and challenged with rec4E1, sc-4E, or unrelated (unr) antibodies. Images were taken after 8 h of growth in complete medium. Scale bar, 100 μm. D: The total tube length, number of tubes, and junction points were quantified using ImageJ following the Matrigel tube formation assay, as described in C. Representative images were analyzed using the Angiogenesis Analyzer plug-in for ImageJ. $^{*}P < 0.05$; paired *t*-test. E: Representative images of sprouts emerging from the choroids of B-hCD93 mice and embedded in Matrigel containing 500 nM of anti-CD93 4E1 derivatives (rec4E1 or sc-4E) or unrelated antibodies (unr). Scale bar, 100 μm. F: Quantitative analysis of the sprouting area from the edge of mouse choroidal tissue. Data are presented as box-and-whisker plots and scatterplots ($n = 18$ explants per condition from 6 different mice). $^{****}P < 0.0001$; unpaired *t*-test.

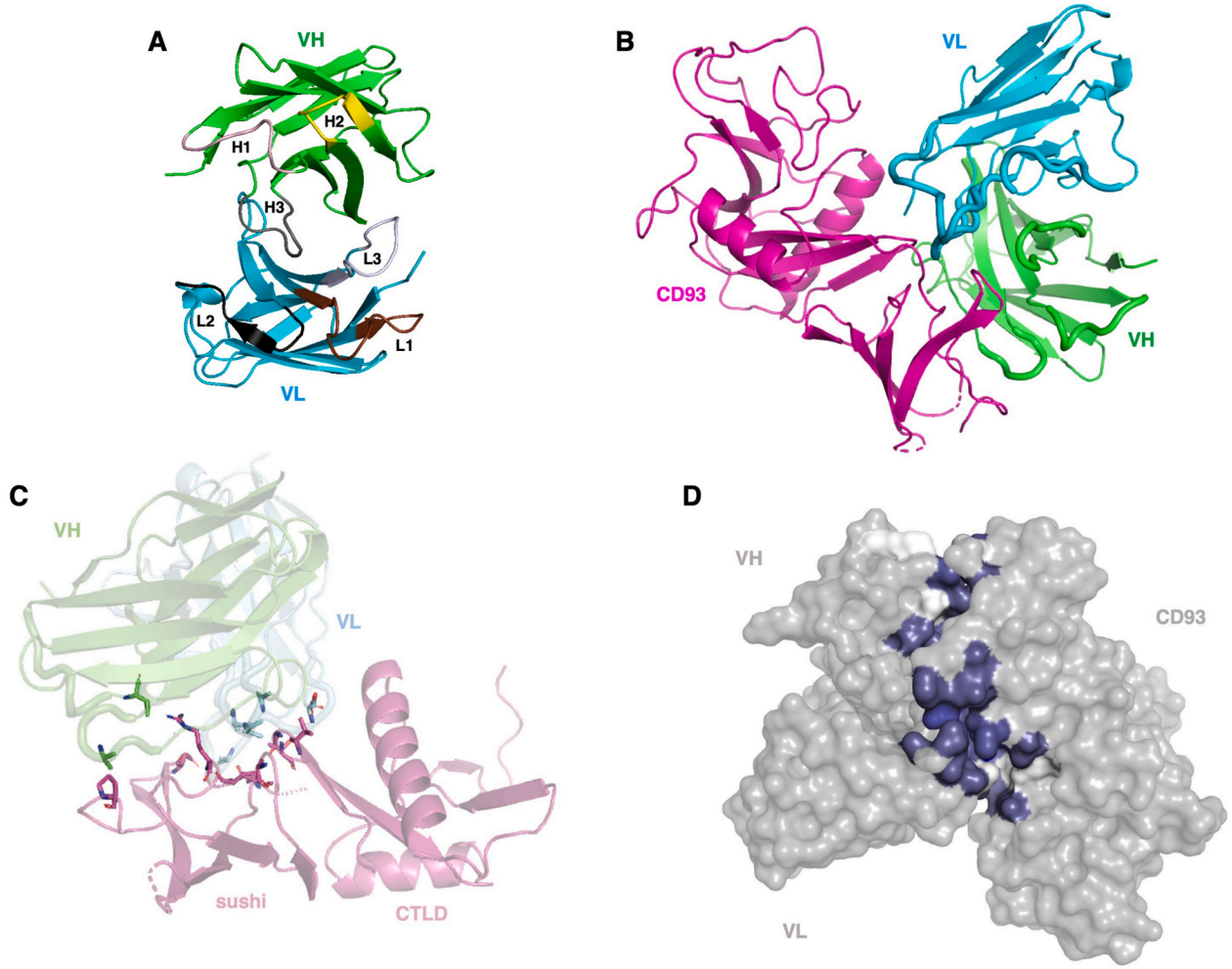

Fig. 4. Overall structure of modeled 4E1 and its interaction with CD93. A: Cartoon representation of the 3D structure of 4E1m. The VH chain is colored green, and the VL chain is colored cyan. The CDRs (H1, H2, H3, and L1, L2, L3) are indicated. B: Molecular docking representation of the 4E1m-CD93 complex obtained using LightDock. The CTLD-sushi domains of CD93 are pseudocolored magenta, while the VH and VL chains of 4E1 are shown in green and cyan, respectively. C: Cartoon representation of the amino acid residues of 4E1m interacting with the CTLD-sushi domains of CD93. Protein domains are labeled and colored as in A. D: Surface analysis of the docked 4E1m-CD93 complex using the Surfaces tool. Blue indicates the most favorable interactions, while white represents less favorable ones. (For interpretation of the references to color in this figure legend, the reader is referred to the web version of this article.)

Table 3
CDR interactions of the 4E1m or sc-4E crystal with the CTLD-sushi domains of CD93.

	4E1 model	sc-4E crystal
CDR-H1	GYTFASY	**GYTFASY**
CDR-H2	**Y**PGNG**D**	**Y**PGN**G**D
CDR-H3	LDWYFDL	L**DWYFD**L
CDR-L1	KAS**Q**SV**DY**DG**D**S**Y**MN	KASQSV**DY**D**G**DS**Y**MN
CDR-L2	AASNLES	AA**SNLES**
CDR-L3	QQN**NE**DPRT	QQN**NE**D**P**R**T**

The interacting amino acid residues, in bold, were identified by integrating PDBsum and PRODIGY analyses.

Docking studies performed using LightDock between the crystal structures of CD93 and sc-4E revealed a potential interaction complex (Fig. 7A). Importantly, cross-referencing the PDBsum and PRODIGY analyses of the docked complex, characterized by strong binding affinity (ΔG, −8.9 kcal/mol), identified the key amino acid residues involved in the binding (Fig. 7B and Table 3), demonstrating that all CDRs of sc-4E contribute to the interaction with CD93. These results were further substantiated by molecular dynamics analyses, confirming the stability of the identified interactions (Fig. S8 and Table S3). Notably, consistent with the previous findings on key residues involved in the binding, the analysis of the average structure of the complex, derived from molecular dynamics simulations and examined using the Surfaces tool, revealed that the interaction surface predominantly involves the CDR-H3 and CDR-L2 regions engaging with the sushi-like domain of CD93 (Fig. 7C).

4. Discussion

The EC-specific receptor CD93 has recently emerged as a pivotal regulator of angiogenesis, interacting with extracellular matrix components such as Multimerin-2 to promote EC adhesion, migration, and differentiation [8,13,14,49]. Targeting CD93 with the monoclonal antibody 4E1 in proliferating ECs has been shown to effectively block angiogenesis without compromising the survival of quiescent cells [6]. Notably, in the choroid, CD93 is selectively expressed on disease-associated vessels from AMD patients, whereas its expression in healthy choroidal vessels is faint [11]. By disrupting the CD93/Multimerin-2 interaction, 4E1 effectively inhibits the growth of choroidal ECs [18], suggesting that interfering with CD93-mediated extracellular matrix interactions in neovascularized choroidal tissue could provide a promising therapeutic strategy for AMD patients. In this context, we have further characterized the monoclonal antibody 4E1,

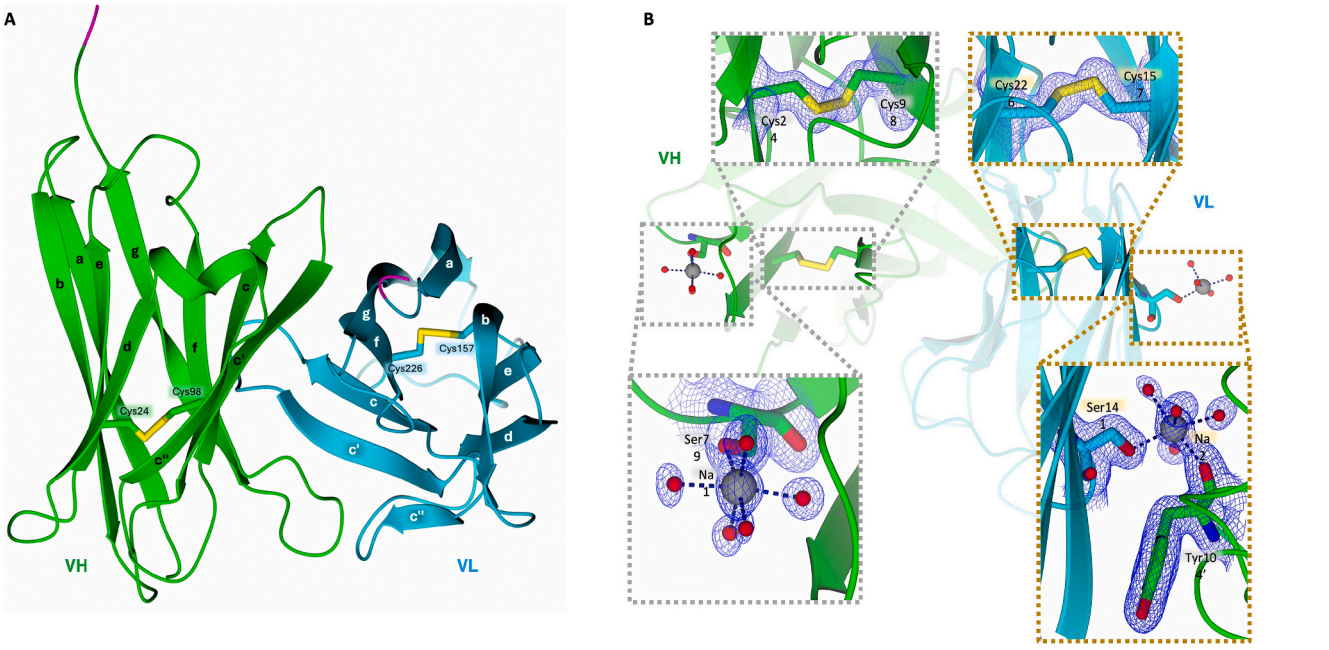

Fig. 5. Crystallographic structure of sc-4E. A: Folding of the scFv VH (green) and VL (cyan) regions. The flexible peptide linker (magenta), spanning residues 120–134, is mostly disordered, and the segment 121–133 was not rebuilt. Both the VH and VL regions are stabilized by disulfide bridges, C24-C98 in VH and C157-C226 in VL (shown as sticks), connecting strands b and f, respectively. B: Main structural features of the VH (green) and VL (cyan) regions of sc-4E. Magnification of the disulfide bridges C24-C98 (VH) and C157-C226 (VL) is shown in the upper insets. Two sodium cations (grey spheres of arbitrary radius) are bound to the VH and VL regions (magnified in the lower insets). In the VH, Na1 is anchored to S79 and is octahedrally coordinated by five additional water molecules. Na2 bridges VL S141 and VH Y104' of a symmetry-related molecule, contributing to crystal packing stabilization. Residues (shown as sticks, color-coded by protein region), water molecules (red sphere), and sodium cations are surrounded by the $2F_o$-F_c map, contoured at the 1.5 σ-level. Coordination bonds are represented as dark blue dashed lines. (For interpretation of the references to color in this figure legend, the reader is referred to the web version of this article.)

optimizing its format and elucidating its binding and inhibitory properties. Our findings demonstrate that the recombinant whole Ig form of 4E1 (rec4E1) retains the binding specificity of the original monoclonal antibody, highlighting its potential as a robust tool for CD93-targeted therapies in AMD treatment. Furthermore, the generation of rec4E1 as a scFv demonstrated comparable binding activity. Compared to full-length antibodies, scFvs offer advantages in terms of manufacturability, reduced immunogenicity, and improved tissue accessibility [22]. The recent approval by the Food and Drug Administration and the European Medicines Agency of brolucizumab, a scFv blocking VEGF-A for the treatment of neovascular AMD, has paved the way for the design of new recombinant molecules specifically for intraocular use in humans [50]. Indeed, clinical trials have proven the therapeutic efficacy of brolucizumab for neovascular AMD by reducing the treatment burden associated with the disease, while maintaining an overall well-tolerated safety profile [51]. Notably, both rec4E1 and sc-4E were shown to inhibit key angiogenic processes in *in vitro* and *ex vivo* experiments, further corroborating prior studies identifying CD93 as a functional mediator of angiogenesis and reinforcing the potential of 4E1 derivatives as effective inhibitors of the CD93/extracellular matrix interaction and, consequently, of pathological angiogenesis in ocular vascular diseases [14,18].

The structural characterization of the variable domains of 4E1, achieved through machine learning-based modeling and X-ray crystallography of sc-4E, represents a significant advancement in understanding the molecular underpinnings of the 4E1-CD93 interaction. Structural insights into antibody-antigen interactions are crucial for understanding antibody binding mechanisms and optimizing their design for therapeutic purposes. The high degree of correspondence between the predicted 4E1 model and the sc-4E crystal structure, particularly within the CDRs, underscores the reliability of computational approaches for antibody engineering [52]. However, the structural deviation observed in the CDR-H3 loop between the predictive model and the crystallographic structure reflects the general inherent flexibility of this region, a feature that often plays a central role in antigen recognition and binding affinity [53]. These findings emphasize the importance of integrating experimental and computational approaches for accurate epitope mapping and rational antibody development.

Crystallographic analyses indicate that sc-4E does not form stable complexes in solution. The dimeric state observed through size-exclusion chromatography is likely a result of transient aggregations of adjacent macromolecules, driven by the high protein concentration of the sample, suggesting that dimerization is not an intrinsic property of sc-4E but rather an artifact caused by the experimental conditions. Furthermore, the analysis of the crystal structure of sc-4E across a wide range of pH values demonstrates its remarkable stability, highlighting its structural robustness.

By integrating structural modeling and docking approaches, this research provides a detailed characterization of 4E1-CD93 interactions, with a particular focus on the structural determinants of binding in the CDR loops. Interestingly, while the predictions based on the modeled structure indicated that three CDRs were engaged in CD93 binding, those based on crystallographic data revealed that all six CDRs of sc-4E contribute to the interaction. Docking and molecular dynamics simulations further highlighted the critical role of the CDR-H3 and CDR-L2 regions, which predominantly interact with the sushi-like domain of CD93. Since the sushi-like domain mediates extracellular matrix interactions, targeting this region could effectively disrupt angiogenic signaling pathways, further reinforcing the therapeutic potential of CD93 blockade [12,18]. However, while docking provides valuable

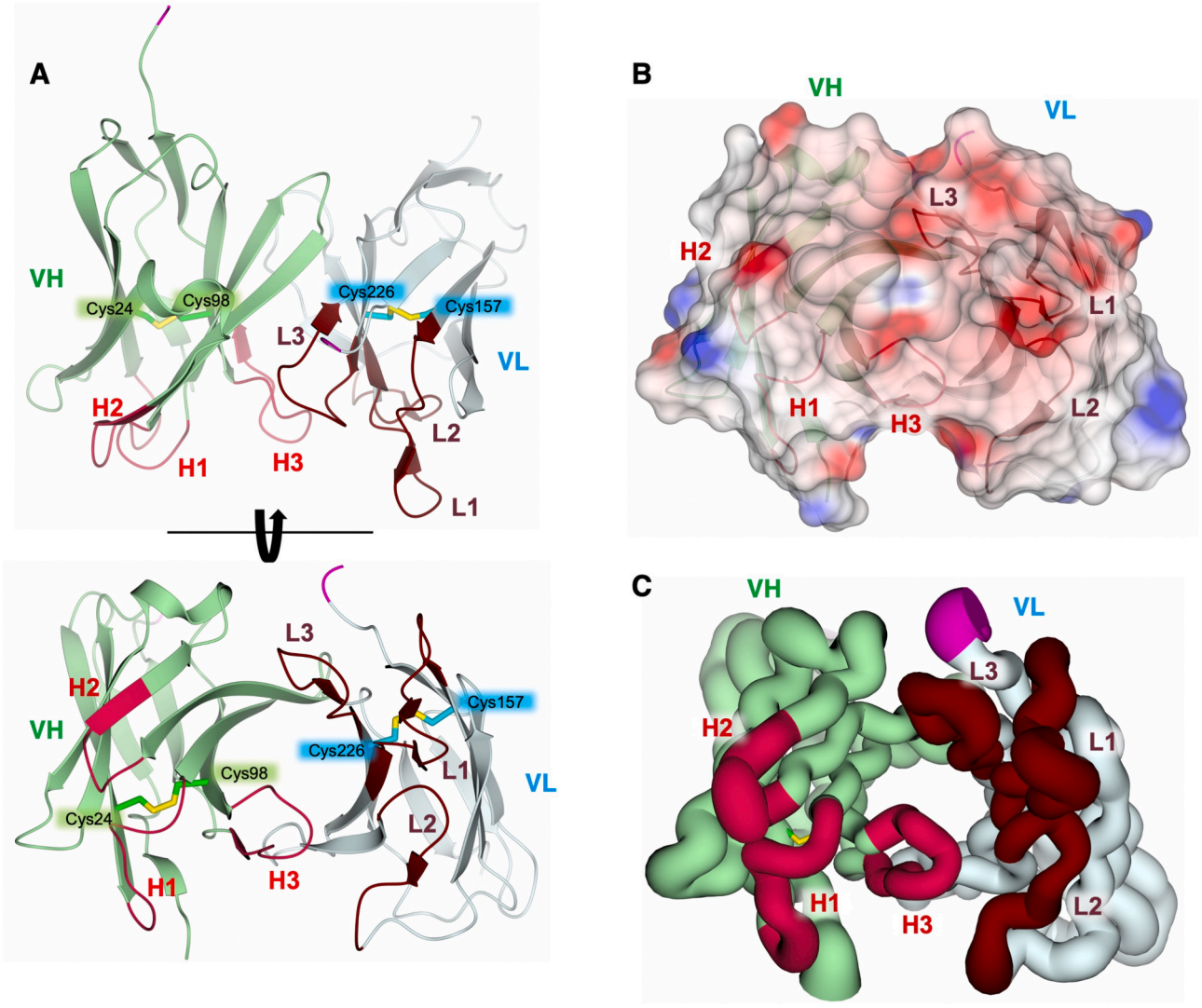

Fig. 6. Analysis of the CDR surface in the sc-4E crystal. A: Cartoon representation of the CDRs (H1, H2, H3, and L1, L2, L3) in the VH (pale green) and VL (pale cyan) regions of the sc-4E structure. The flexible peptide linker is shown in magenta. B: Surface view of sc-4E. Protein areas are color-coded based on their local electrostatic potential: neutral regions are shown in white, while negatively and positively charged areas are represented in red and blue, respectively. CDRs are indicated. C: The sc-4E structure is depicted using a worm representation scaled by atomic B-factors. The residues forming the CDRs in both regions exhibit atomic B-factors close to the protein's average, indicating low flexibility. The only exception is the central portion of CDR-L1, which shows slightly increased flexibility, as reflected by the increased worm thickness. (For interpretation of the references to color in this figure legend, the reader is referred to the web version of this article.)

predictive insights, it may not fully capture the precise molecular interactions observed in co-crystallized CD93-antibody complexes. Nonetheless, the strong synergy between bioinformatics modeling and experimental validation underscores the transformative potential of machine learning-based antibody engineering in therapeutic development. These advancements are particularly significant in addressing global disparities in access to advance biologics. Given the widespread impact of angiogenesis-driven diseases, machine learning-assisted antibody design could accelerate the development of next-generation biomedicine, making them more adaptable to diverse healthcare settings, including periurban and underserved regions [20].

In conclusion, our in-depth characterization of 4E1 in both its recombinant and scFv formats, combined with structural insights into its interaction with CD93, lays the foundations for the development of CD93-targeted therapies. By inhibiting CD93, these tools have the potential to open new avenues for innovative anti-angiogenic strategies.

Glossary

AMD	age-related macular degeneration
CD93	cluster of differentiation 93
CTLD	C-type lectin-like domain
EC	endothelial cell
VH and VL	variable heavy and light chains
CDR	complementary determining region
scFv	single-chain antibody fragment
CHO	chinese hamster ovary
FBS	fetal bovine serum
HEK	human embryonic kidney
HUVEC	human umbilical vein endothelial cell
PBS	phosphate-buffered saline
HPR	horseradish peroxidase
BSA	bovine serum albumin
PDB	protein data bank
FDA	Food and Drug Administration
EMA	European Medicines Agency

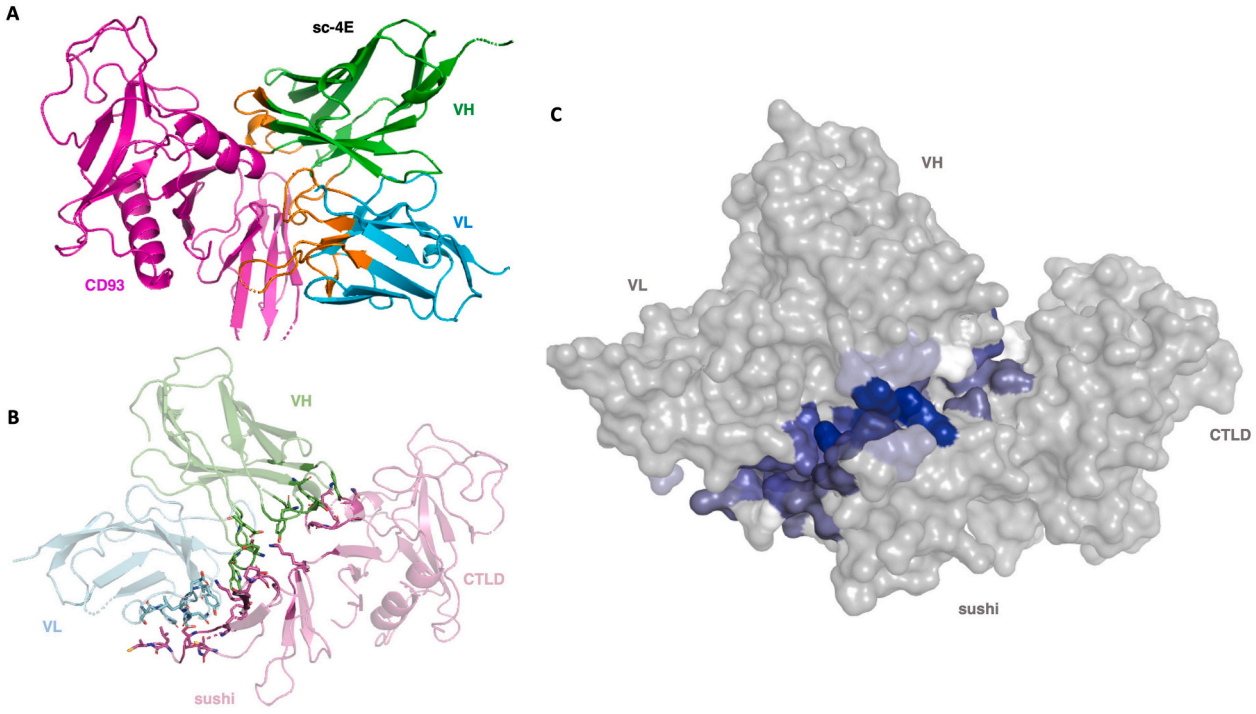

Fig. 7. Model of the sc-4E-CD93 interaction. A: Cartoon representation of the molecular docking of the sc-4E/CD93 complex. The CTLD-sushi domains of CD93 are pseudocolored in magenta. The VH and VL of sc-4E are shown in green and cyan, respectively. The CDRs of sc-4E are highlighted in orange. B: Licorice representation of the interactions between sc-4E and the CTLD-sushi domains of CD93. Protein domains are labeled and pseudocolored as in A. C: Interacting surfaces of the docked sc-4E/CD93 complex are color-coded, with blue indicating the most favorable interactions and white representing less favorable ones. Favorable interactions (blue) involve residues in the CDRs H2 and L3 and the sushi-like domain. (For interpretation of the references to color in this figure legend, the reader is referred to the web version of this article.)

CSA choroid sprouting assay

CRediT authorship contribution statement

Luisa Raucci: Writing – review & editing, Methodology, Investigation, Funding acquisition, Data curation. **Cosimo Damiano Perrone:** Software, Methodology, Investigation. **Stefano Barbera:** Writing – review & editing, Investigation. **Laurens Julius de Boer:** Software, Methodology, Investigation. **Gian Marco Tosi:** Writing – review & editing, Funding acquisition. **Jlenia Brunetti:** Writing – review & editing, Investigation. **Luisa Bracci:** Writing – review & editing, Resources. **Cecilia Pozzi:** Writing – review & editing, Validation, Supervision, Resources, Methodology, Data curation. **Federico Galvagni:** Writing – review & editing, Validation, Resources, Funding acquisition, Conceptualization. **Maurizio Orlandini:** Writing – original draft, Visualization, Validation, Supervision, Resources, Funding acquisition, Data curation, Conceptualization.

Fundings

This work was supported by the European-Union, Next Generation EU, Tuscany Health Ecosystem, Spoke 7 (grant number CUP BC63C22000680007); and the University of Siena, New Frontiers (grant number 2265-2023-RL-PSR-FNF2023_001).

Declaration of competing interest

The sequences encoding for the antibody 4E1 are covered by a patent owned by UCme Bioscience srl. Gian Marco Tosi, Federico Galvagni, and Maurizio Orlandini are partners of UCme Bioscience srl. The rest of the authors declare that they have no other competing financial interests.

Acknowledgements

The authors would like to express their gratitude to Prof. A. Bernini (University of Siena) for his invaluable assistance with the molecular dynamics experiments. Moreover, we thank the European Synchrotron Radiation Facility (ESRF, proposal MX2658), the PETRA III (proposal mx956), and the Diamond Light Source (DLS, proposal MX36130) synchrotrons for beamtime. We also acknowledge the staff of the DLS beamline I04, the PetraIII beamline P13 and the ESRF beamline ID30A-3 for their assistance during beamtime. Particularly, we would like to thank our local contacts at PetraIII P13, Dr. I. Bento, DLS I04, Dr. D. Aragao, and ESRF ID30A-3, Dr. P. Carpentier. Finally, we sincerely thank Dr. M. Lorenzoni for his valuable advice and continuous support throughout our research.

Appendix A. Supplementary data

Supplementary data to this article can be found online at https://doi.org/10.1016/j.ijbiomac.2025.143118.

References

[1] S.R. Flaxman, R.R.A. Bourne, S. Resnikoff, P. Ackland, T. Braithwaite, M. V Cicinelli, A. Das, J.B. Jonas, J. Keeffe, J.H. Kempen, J. Leasher, H. Limburg, K. Naidoo, K. Pesudovs, A. Silvester, G.A. Stevens, N. Tahhan, T.Y. Wong, H. R. Taylor, R. Bourne, P. Ackland, A. Arditi, Y. Barkana, B. Bozkurt, T. Braithwaite, A. Bron, D. Budenz, F. Cai, R. Casson, U. Chakravarthy, J. Choi, M.V. Cicinelli, N. Congdon, R. Dana, R. Dandona, L. Dandona, A. Das, I. Dekaris, M. Del Monte, J. Deva, L. Dreer, L. Ellwein, M. Frazier, K. Frick, D. Friedman, J. Furtado, H. Gao, G. Gazzard, R. George, S. Gichuhi, V. Gonzalez, B. Hammond, M.E. Hartnett, M. He, J. Hejtmancik, F. Hirai, J. Huang, A. Ingram, J. Javitt, J. Jonas, C. Joslin, J. Keeffe, J. Kempen, M. Khairallah, R. Khanna, J. Kim, G. Lambrou, V.C. Lansingh, P. Lanzetta, J. Leasher, J. Lim, H. LIMBURG, K. Mansouri, A. Mathew, A. Morse, B. Munoz, D. Musch, K. Naidoo, V. Nangia, M. Palaiou, M.B. Parodi, F.Y. Pena, K. Pesudovs, T. Peto, H. Quigley, M. Raju, P. Ramulu, Z. Rankin, S. Resnikoff, D. Reza, A. Robin, L. Rossetti, J. Saaddine, M. Sandar, J. Serle, T. Shen, R. Shetty,

P. Sieving, J.C. Silva, A. Silvester, R.S. Sitorus, D. Stambolian, G. Stevens, H. Taylor, J. Tejedor, J. Tielsch, M. Tsilimbaris, J. van Meurs, R. Varma, G. Virgili, Y.X. Wang, N.-L. Wang, S. West, P. Wiedemann, T. Wong, R. Wormald, Y. Zheng, Global causes of blindness and distance vision impairment 1990–2020: a systematic review and meta-analysis, Lancet Glob. Health 5 (2017) e1221–e1234, https://doi.org/10.1016/S2214-109X(17)30393-5.

[2] P. Mammadzada, P.M. Corredoira, H. André, The role of hypoxia-inducible factors in neovascular age-related macular degeneration: a gene therapy perspective, Cell. Mol. Life Sci. 77 (2020) 819–833, https://doi.org/10.1007/s00018-019-03422-9.

[3] R.H. Foxton, S. Uhles, S. Grüner, F. Revelant, C. Ullmer, Efficacy of simultaneous VEGF-A/ANG-2 neutralization in suppressing spontaneous choroidal neovascularization, EMBO Mol. Med. 11 (2019) e10204, https://doi.org/10.15252/emmm.201810204.

[4] S. Barbera, C. Cucini, A glimpse into the past: phylogenesis and protein domain analysis of the group XIV of C-type lectins in vertebrates, BMC Genomics 23 (2022) 420, https://doi.org/10.1186/s12864-022-08659-6.

[5] A.N. Zelensky, J.E. Gready, The C-type lectin-like domain superfamily, FEBS J. 272 (2005) 6179–6217, https://doi.org/10.1111/j.1742-4658.2005.05031.x.

[6] M. Orlandini, F. Galvagni, M. Bardelli, M. Rocchigiani, C. Lentucci, F. Anselmi, A. Zippo, L. Bini, S. Oliviero, The characterization of a novel monoclonal antibody against CD93 unveils a new antiangiogenic target, Oncotarget 5 (2014) 2750–2760.

[7] F. Galvagni, F. Nardi, M. Maida, G. Bernardini, S. Vannuccini, F. Petraglia, A. Santucci, M. Orlandini, CD93 and dystroglycan cooperation in human endothelial cell adhesion and migration, Oncotarget 7 (2016) 10090–10103, https://doi.org/10.18632/oncotarget.7136.

[8] S. Barbera, R. Lugano, A. Pedalina, M. Mongiat, A. Santucci, G.M. Tosi, A. Dimberg, F. Galvagni, M. Orlandini, The C-type lectin CD93 controls endothelial cell migration via activation of the rho family of small GTPases, Matrix Biol. 99 (2021) 1–17, https://doi.org/10.1016/j.matbio.2021.05.006.

[9] M. Masiero, F.C. Simões, H.D. Han, C. Snell, T. Peterkin, E. Bridges, L.S. Mangala, S.Y.-Y. Wu, S. Pradeep, D. Li, C. Han, H. Dalton, G. Lopez-Berestein, J.B. Tuynman, N. Mortensen, J.-L. Li, R. Patient, A.K. Sood, A.H. Banham, A.L. Harris, F.M. Buffa, A core human primary tumor angiogenesis signature identifies the endothelial orphan receptor ELTD1 as a key regulator of angiogenesis, Cancer Cell 24 (2013) 229–241, https://doi.org/10.1016/j.ccr.2013.06.004.

[10] K. Vemuri, B. de Alves Pereira, P. Fuenzalida, Y. Subashi, S. Barbera, L. van Hooren, M. Hedlund, F. Pontén, C. Lindskog, A.-K. Olsson, R. Lugano, A. Dimberg, CD93 maintains endothelial barrier function and limits metastatic dissemination, JCI, Insight 9 (2024) e169830, https://doi.org/10.1172/jci.insight.169830.

[11] G.M. Tosi, E. Caldi, B. Parolini, P. Toti, G. Neri, F. Nardi, C. Traversi, G. Cevenini, D. Marigliani, E. Nuti, T. Bacci, F. Galvagni, M. Orlandini, CD93 as a potential target in neovascular age-related macular degeneration, J. Cell. Physiol. 232 (2017) 1767–1773, https://doi.org/10.1002/jcp.25689.

[12] F. Galvagni, F. Nardi, O. Spiga, A. Trezza, G. Tarticchio, R. Pellicani, E. Andreuzzi, E. Caldi, P. Toti, G.M. Tosi, A. Santucci, R.V. Iozzo, M. Mongiat, M. Orlandini, Dissecting the CD93-Multimerin 2 interaction involved in cell adhesion and migration of the activated endothelium, Matrix Biol. 64 (2017) 112–127, https://doi.org/10.1016/j.matbio.2017.08.003.

[13] K.A. Khan, A.J. Naylor, A. Khan, P.J. Noy, M. Mambretti, P. Lodhia, J. Athwal, A. Korzystka, C.D. Buckley, B.E. Willcox, F. Mohammed, R. Bicknell, Multimerin-2 is a ligand for group 14 family C-type lectins CLEC14A, CD93 and CD248 spanning the endothelial pericyte interface, Oncogene 36 (2017) 6097–6108, https://doi.org/10.1038/onc.2017.214.

[14] S. Barbera, F. Nardi, I. Elia, G. Realini, R. Lugano, A. Santucci, G.M. Tosi, A. Dimberg, F. Galvagni, M. Orlandini, The small GTPase Rab5c is a key regulator of trafficking of the CD93/Multimerin-2/β1 integrin complex in endothelial cell adhesion and migration, Cell Commun. Signal 17 (2019) 55, https://doi.org/10.1186/s12964-019-0375-x.

[15] S. Barbera, L. Raucci, R. Lugano, G.M. Tosi, A. Dimberg, A. Santucci, F. Galvagni, M. Orlandini, CD93 signaling via rho proteins drives cytoskeletal remodeling in spreading endothelial cells, Int. J. Mol. Sci. 22 (2021) 12417, https://doi.org/10.3390/ijms222212417.

[16] R. Lugano, K. Vemuri, D. Yu, M. Bergqvist, A. Smits, M. Essand, S. Johansson, E. Dejana, A. Dimberg, CD93 promotes β1 integrin activation and fibronectin fibrillogenesis during tumor angiogenesis, J. Clin. Invest. 128 (2018) 3280–3297, https://doi.org/10.1172/JCI97459.

[17] S. Zanivan, F. Maione, M.Y. Hein, J.R. Herná Ndez-Fernaud, P. Ostasiewicz, E. Giraudo, M. Mann, Silac-based proteomics of human primary endothelial cell morphogenesis unveils tumor angiogenic markers, Mol. Cell. Proteomics 12 (2013) 3599–3611, https://doi.org/10.1074/mcp.M113.031344.

[18] G.M. Tosi, G. Neri, S. Barbera, L. Mundo, B. Parolini, S. Lazzi, R. Lugano, E. Poletto, L. Leoncini, G. Pertile, M. Mongiat, A. Dimberg, F. Galvagni, M. Orlandini, The binding of CD93 to Multimerin-2 promotes choroidal neovascularization, Invest. Ophthalmol. Vis. Sci. 61 (2020) 30, https://doi.org/10.1167/IOVS.61.8.30.

[19] S. Barbera, L. Raucci, G. Tassone, L. Tinti, F. Prischi, A. Santucci, M. Mongiat, G. M. Tosi, F. Galvagni, A. Dimberg, C. Pozzi, M. Orlandini, Dimerization of the C-type lectin-like receptor CD93 promotes its binding to Multimerin-2 in endothelial cells, Int. J. Biol. Macromol. 224 (2023) 453–464, https://doi.org/10.1016/j.ijbiomac.2022.10.136.

[20] S. Koley, Critically reckoning spectrophotometric detection of asymptomatic cyanotoxins and faecal contamination in periurban agrarian ecosystems via convolutional neural networks, Trends Sci. 21 (2024) 8528, https://doi.org/10.48048/tis.2024.8528.

[21] L. Li, E. Gupta, J. Spaeth, L. Shing, R. Jaimes, E. Engelhart, R. Lopez, R.S. Caceres, T. Bepler, M.E. Walsh, Machine learning optimization of candidate antibody yields highly diverse sub-nanomolar affinity antibody libraries, Nat. Commun. 14 (2023) 3454, https://doi.org/10.1038/s41467-023-39022-2.

[22] Z.A. Ahmad, S.K. Yeap, A.M. Ali, W.Y. Ho, N.B.M. Alitheen, M. Hamid, scFv antibody: principles and clinical application, Clin. Dev. Immunol. 2012 (2012) 980250, https://doi.org/10.1155/2012/980250.

[23] C. Chothia, A.M. Lesk, A. Tramontano, M. Levitt, S.J. Smith-Gill, G. Air, S. Sheriff, E.A. Padlan, D. Davies, W.R. Tulip, P.M. Colman, S. Spinelli, P.M. Alzari, R. J. Poljak, Conformations of immunoglobulin hypervariable regions, Nature 342 (1989) 877–883, https://doi.org/10.1038/342877a0.

[24] L. Li, S. Chen, Z. Miao, Y. Liu, X. Liu, Z.-X. Xiao, Y. Cao, AbRSA: a robust tool for antibody numbering, Protein Sci. 28 (2019) 1524–1531, https://doi.org/10.1002/pro.3633.

[25] M. Orlandini, S. Nucciotti, F. Galvagni, M. Bardelli, M. Rocchigiani, F. Petraglia, S. Oliviero, Morphogenesis of human endothelial cells is inhibited by DAB2 via Src, FEBS Lett. 582 (2008) 2542–2548, https://doi.org/10.1016/j.febslet.2008.06.025.

[26] F. Galvagni, F. Anselmi, A. Salameh, M. Orlandini, M. Rocchigiani, S. Oliviero, Vascular endothelial growth factor receptor-3 activity is modulated by its association with caveolin-1 on endothelial membrane, Biochemistry 46 (2007), https://doi.org/10.1021/bi061400n.

[27] B. Abanades, G. Georges, A. Bujotzek, C.M. Deane, ABlooper: fast accurate antibody CDR loop structure prediction with accuracy estimation, Bioinformatics 38 (2022) 1877–1880, https://doi.org/10.1093/bioinformatics/btac016.

[28] B. Abanades, W.K. Wong, F. Boyles, G. Georges, A. Bujotzek, C.M. Deane, ImmuneBuilder: deep-learning models for predicting the structures of immune proteins, Commun. Biol. 6 (2023) 575, https://doi.org/10.1038/s42003-023-04927-7.

[29] J. Roel-Touris, A.M.J.J. Bonvin, B. Jiménez-García, LightDock goes information-driven, Bioinformatics 36 (2020) 950–952, https://doi.org/10.1093/bioinformatics/btz642.

[30] R.A. Laskowski, E.G. Hutchinson, A.D. Michie, A.C. Wallace, M.L. Jones, J. M. Thornton, PDBsum: a web-based database of summaries and analyses of all PDB structures, Trends Biochem. Sci. 22 (1997) 488–490, https://doi.org/10.1016/S0968-0004(97)01140-7.

[31] L.C. Xue, J.P. Rodrigues, P.L. Kastritis, A.M. Bonvin, A. Vangone, PRODIGY: a web server for predicting the binding affinity of protein–protein complexes, Bioinformatics 32 (2016) 3676–3678, https://doi.org/10.1093/bioinformatics/btw514.

[32] M.J. Abraham, T. Murtola, R. Schulz, S. Páll, J.C. Smith, B. Hess, E. Lindahl, GROMACS: high performance molecular simulations through multi-level parallelism from laptops to supercomputers, SoftwareX 1–2 (2015) 19–25, https://doi.org/10.1016/j.softx.2015.06.001.

[33] N. Teruel, V.M. Borges, R. Najmanovich, Surfaces: a software to quantify and visualize interactions within and between proteins and ligands, Bioinformatics 39 (2023) btad608, https://doi.org/10.1093/bioinformatics/btad608.

[34] M. Benvenuti, S. Mangani, Crystallization of soluble proteins in vapor diffusion for x-ray crystallography, Nat. Protoc. 2 (2007) 1633–1651, https://doi.org/10.1038/nprot.2007.198.

[35] W. Kabsch, XDS, Acta Crystallogr., D Biol, Crystallogr 66 (2010) 125–132.

[36] P.R. Evans, An introduction to data reduction: space-group determination, scaling and intensity statistics, Acta Crystallogr. D Biol. Crystallogr. 67 (2011) 282–292, https://doi.org/10.1107/S090744491003982X.

[37] M.D. Winn, C.C. Ballard, K.D. Cowtan, E.J. Dodson, P. Emsley, P.R. Evans, R. M. Keegan, E.B. Krissinel, A.G.W. Leslie, A. McCoy, S.J. McNicholas, G. N. Murshudov, N.S. Pannu, E.A. Potterton, H.R. Powell, R.J. Read, A. Vagin, K. S. Wilson, Overview of the CCP4 suite and current developments, Acta Crystallogr. D Biol. Crystallogr. 67 (2011) 235–242, https://doi.org/10.1107/S0907444910045749.

[38] A. Vagin, A. Teplyakov, Molecular replacement with MOLREP, Acta Crystallogr. D Biol. Crystallogr. 66 (2010) 22–25, https://doi.org/10.1107/S0907444909042589.

[39] G.N. Murshudov, P. Skubák, A.A. Lebedev, N.S. Pannu, R.A. Steiner, R.A. Nicholls, M.D. Winn, F. Long, A.A. Vagin, REFMAC5 for the refinement of macromolecular crystal structures, Acta Crystallogr. D Biol. Crystallogr. 67 (2011) 355–367, https://doi.org/10.1107/S0907444911001314.

[40] G. Langer, S.X. Cohen, V.S. Lamzin, A. Perrakis, Automated macromolecular model building for X-ray crystallography using ARP/wARP version 7, Nat. Protoc. 3 (2008) 1171–1179, https://doi.org/10.1038/nprot.2008.91.

[41] P. Emsley, B. Lohkamp, W.G. Scott, K. Cowtan, Features and development of coot, Acta Crystallogr. D Biol. Crystallogr. 66 (2010) 486–501, https://doi.org/10.1107/S0907444910007493.

[42] R.M.M.M.D. and T.J. Laskowski, PROCHECK: a program to check the stereochemical quality of protein structures, J. Appl. Crystallogr. 26 (1993) 283–291.

[43] L. Potterton, S. McNicholas, E. Krissinel, J. Gruber, K. Cowtan, P. Emsley, G. N. Murshudov, S. Cohen, A. Perrakis, M. Noble, Developments in the CCP4 molecular-graphics project, Acta Crystallogr. D Biol. Crystallogr. 60 (2004) 2288–2294, https://doi.org/10.1107/S0907444904023716.

[44] A. Frenzel, M. Hust, T. Schirrmann, Expression of recombinant antibodies, Front. Immunol. 4 (2013) 217. https://www.frontiersin.org/articles/https://doi.org/10.3389/fimmu.2013.00217.

[45] P. Holliger, P.J. Hudson, Engineered antibody fragments and the rise of single domains, Nat. Biotechnol. 23 (2005) 1126–1136, https://doi.org/10.1038/nbt1142.

[46] A. Singh, V. Upadhyay, A.K. Panda, Solubilization and refolding of inclusion body proteins, in: E. García-Fruitós (Ed.), Methods Mol. Biol, Springer, New York, New York, NY, 2015, pp. 283–291, https://doi.org/10.1007/978-1-4939-2205-5_15.

[47] Z. Shao, M. Friedlander, C.G. Hurst, Z. Cui, D.T. Pei, L.P. Evans, A.M. Juan, H. Tahir, F. Duhamel, J. Chen, P. Sapieha, S. Chemtob, J.-S. Joyal, L.E.H. Smith, Choroid sprouting assay: an ex vivo model of microvascular angiogenesis, PLoS One 8 (2013) e69552-. doi:https://doi.org/10.1371/journal.pone.0069552.

[48] E. Krissinel, K. Henrick, Inference of macromolecular assemblies from crystalline state, J. Mol. Biol. 372 (2007) 774–797, https://doi.org/10.1016/j.jmb.2007.05.022.

[49] Y. Sun, W. Chen, R.J. Torphy, S. Yao, G. Zhu, R. Lin, R. Lugano, E.N. Miller, Y. Fujiwara, L. Bian, L. Zheng, S. Anand, F. Gao, W. Zhang, S.E. Ferrara, A. E. Goodspeed, A. Dimberg, X.J. Wang, B.H. Edil, C.C. Barnett, R.D. Schulick, L. Chen, Y. Zhu, Blockade of the CD93 pathway normalizes tumor vasculature to facilitate drug delivery and immunotherapy, Sci. Transl. Med. 13 (2021) eabc8922, https://doi.org/10.1126/scitranslmed.abc8922.

[50] Q.D. Nguyen, A. Das, D.V. Do, P.U. Dugel, A. Gomes, F.G. Holz, A. Koh, C.K. Pan, Y. J. Sepah, N. Patel, H. MacLeod, P. Maurer, Brolucizumab: evolution through preclinical and clinical studies and the implications for the management of neovascular age-related macular degeneration, Ophthalmology 127 (2020) 963–976, https://doi.org/10.1016/j.ophtha.2019.12.031.

[51] P.U. Dugel, R.P. Singh, A. Koh, Y. Ogura, G. Weissgerber, K. Gedif, G.J. Jaffe, R. Tadayoni, U. Schmidt-Erfurth, F.G. Holz, HAWK and HARRIER: ninety-six-week outcomes from the phase 3 trials of brolucizumab for neovascular age-related macular degeneration, Ophthalmology 128 (2021) 89–99, https://doi.org/10.1016/j.ophtha.2020.06.028.

[52] J. Jumper, R. Evans, A. Pritzel, T. Green, M. Figurnov, O. Ronneberger, K. Tunyasuvunakool, R. Bates, A. Žídek, A. Potapenko, A. Bridgland, C. Meyer, S.A. A. Kohl, A.J. Ballard, A. Cowie, B. Romera-Paredes, S. Nikolov, R. Jain, J. Adler, T. Back, S. Petersen, D. Reiman, E. Clancy, M. Zielinski, M. Steinegger, M. Pacholska, T. Berghammer, S. Bodenstein, D. Silver, O. Vinyals, A.W. Senior, K. Kavukcuoglu, P. Kohli, D. Hassabis, Highly accurate protein structure prediction with AlphaFold, Nature 596 (2021) 583–589, https://doi.org/10.1038/s41586-021-03819-2.

[53] M.L. Fernández-Quintero, K.B. Kroell, L.M. Bacher, J.R. Loeffler, P.K. Quoika, G. Georges, A. Bujotzek, H. Kettenberger, K.R. Liedl, Germline-dependent antibody paratope states and pairing specific VH-VL interface dynamics, Front. Immunol. 12 (2021) 675655. https://www.frontiersin.org/journals/immunology/articles/https://doi.org/10.3389/fimmu.2021.675655.